Comparison of Gaussian and Poisson Statistics when Fitting X-Ray Spectra Using Observations of the Small Magellanic Cloud by the Chandra X-Ray Observatory

Bachelorarbeit aus der Physik

Vorgelegt von

Florian Steynberg

8.1.2020

Dr. Karl Remeis-Sternwarte
Friedrich-Alexander-Universität Erlangen-Nürnberg

Betreuerin: Prof. Dr. Manami Sasaki

Abstract

Statistics are one of the most important mathematical tools for all fields of science. Astronomy is no exception to this, and relies heavily on statistics to further the knowledge of the universe. Especially X-ray astronomers often have to cope with significant backgrounds and a lot of noise in their data, which makes statistical methods even more important.
From a physical stand-point, the data were always Poisson distributed, but they can be approximated as Gaussian data for high enough count rates. This approximation allows for easy handling of the background, which can be simply subtracted from the source data. This is not possible for Poisson distributed data. While this approximation may be convenient, the bias it introduces increases, as the count rates gets smaller, which can lead to significant errors in data with low statistics.
For extended sources a subtraction of the background can also introduce an additional error

The source data for this thesis were acquired by the Chandra X-ray Observatory during an observation of the N19 region in the Small Magellanic Cloud. This region is suspected to possibly contain a number of supernova remnants. While not being the focus of this thesis, determining if a source could be a SNR is in part accomplished by analyzing the X-ray spectra.

The aim of this thesis, is to compare the use of Gaussian statistic (χ^2-statistic) to the use of Poisson statistic (Cash statistic) in the spectral analysis of X-ray data. The main goal lies in showing, that using a Poisson statistic results in plausible results, despite requiring a separate model for the background.

Table of Contents

List of Figures

1 Introduction to X-ray astronomy

The following introduction is roughly based on Chapter 1 from Seward and Charles (2010). X-rays were accidentally discovered in 1895 by Wilhelm Conrad Röntgen, when a discharge tube, though being covered with black cardboard, caused a faint glow on a fluorescent screen. After further experimentation, he confirmed the cause to be a new kind of radiation, that could penetrate different kinds of materials. Röntgen, who was awarded the first Nobel Prize in Physics for his discovery, called this new kind of radiation 'X-Strahlen' (X-rays).

We now know X-rays to be a form of electro-magnetic radiation with an energy per photon a thousand times higher than that of visible light. The energy of X-rays is thus usually measured in keV, while that of visible light lies in the eV range. Putting special cases like glass aside, X-rays can penetrate into materials much deeper than light of lower energies. Since the absorption of X-rays increases with the atomic number Z, heavier elements like the Calcium in bones absorb more X-rays than Carbon, Oxygen or Hydrogen in flesh. Röntgen himself recognized the medical use of this property of X-rays by taking the first ever X-ray image of his wife's hand.

Most astronomical X-rays are found at much lower energies (0.5 - 5 keV) than the ones Röntgen used for his image. Practically all of these extra terrestrial X-rays are absorbed by the atmosphere, which makes ground based observations physically impossible. Figure 1.1 depicts the height, respectively the fraction of the atmosphere at which 50% of radiation with a certain wavelength is absorbed. Radio and optical emissions reach the surface nearly unaffected, while X-ray and UV-emissions are already heavily attenuated at heights above 100km.

This strong atmospheric absorption makes ground based observations of X-rays physically impossible, since at 1 atmosphere, only 10 cm of air already absorbs 90% of 3 keV X-rays. To measure astronomical X-rays at all, observations must be conducted above 99% of the atmosphere ($\sim$ 30 km), at which high altitude balloons are able to measure X-rays at an energy range of around 30 keV. The most prominent X-ray band however can only be observed above all but one millionth of the atmosphere ($\sim$ 100km). In this case, rockets must be used, which can reach up to 200 km, where even X-rays below 1 keV can be measured.
Today most X-ray observations are conducted with satellite observatories.

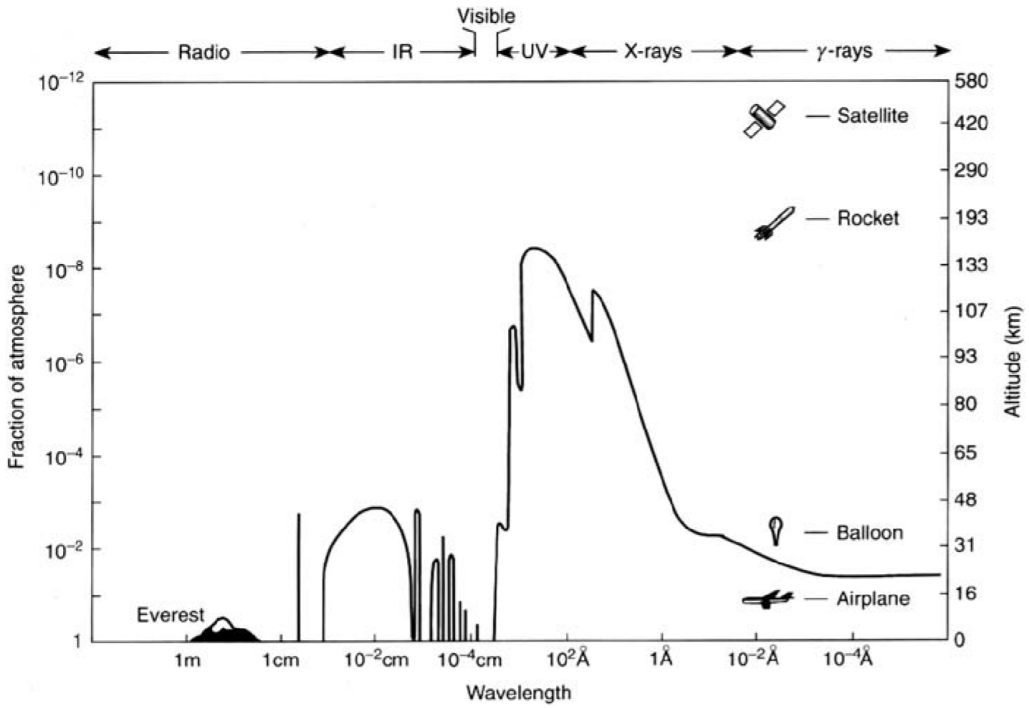

Figure 1.1: Schematic depiction of the transmission of electromagnetic radiation through the atmosphere. The solid line marks the height at which 50% of the radiation with the corresponding wavelength is absorbed. credit: Seward and Charles (2010) Fig. 1.1

The first astronomical X-ray observations occurred after World War II. An important part herein played the infamous V2 rocket, which could be used to carry scientific equipment over 100 km high into the thermosphere. Using a V2 rocket, a group of scientists at the U.S. Naval Research Laboratory (NRL), under Herbert Friedman, was able to show the sun to be a strong X-ray and UV emitter. Ironically, this first discovery of solar X-rays disheartened many astronomers to find any extra-solar X-ray sources, since such sources were expected to be much too faint to be detectable.

These doubts could be dispelled by the discovery made by a group at American Science and Engineering (AS&E) led by Riccardo Giacconi. Tasked with the search for X-rays originating from the moon in the early 1960s, the moon being of particular importance due to the space race, Giacconis team launched a rocket on June 18 1962. While this rocket based observation failed to detect any lunar X-rays, a signal from a strong extra-solar source was measured (Giacconi et al. (1962)). This first cosmic X-ray source was called Sco X-1, named after the constellation Scorpius, where it is located.
Giaconni was awarded the Nobel Prize in Physics 2002 for his important accomplishments in the development of X-ray astronomy.

The detection of Sco X-1 should not remain the only one. Only a few months after this groundbreaking discovery, in October 12 1962, two weaker sources were observed, one being the Crab Nebula, a well known supernova remnant. Astronomers started to realize that there were many more observable cosmic X-ray sources than expected. With rockets and balloons, only small areas in the sky could be explored until December 12 1970, when the Uhuru satellite was launched, and the first comprehensive surveys were undertaken.

Many more satellite based X-ray observatories should follow. The following list names only a few (WKT (2002)):

- High Energy Astronomy Observatory-1 (HEAO-1) (1977): First satellite conducting an all-sky survey.
- Einstein Observatory (1978): First dedicated X-ray satellite with a focusing optic in form of concentric mirrors.
- Röntgensatellite (ROSAT) (1993): Conducted all-sky survey that increased the number of known X-ray sources to 125,000. Took data during the 100th anniversary of the discovery of X-rays.
- Chandra X-ray Observatory (1999): High precision and sensitivity facilitated many astronomical discoveries, especially in the area of supernova remnants.

2 Overview of the Chandra X-ray observatory

The Chandra X-ray observatory was launched on July 23 1999 by the Space Shuttle Columbia. An additional Inertial Upper Stage and Chandra's own internal propulsion systems delivered the observatory into a high elliptical orbit. The apogee height, the orbital distance furthest from earth, was about 129,000 km in 2017. The closest distance to earth, the perigee height, was about 19,000 km which translates to an eccentricity of 0.68. The orbital period of 63.5 h, with 75% of the time spent above the radiation belts surrounding earth, allows in theory for observation times of 170 ks (Chandra IPI Teams (2019)).

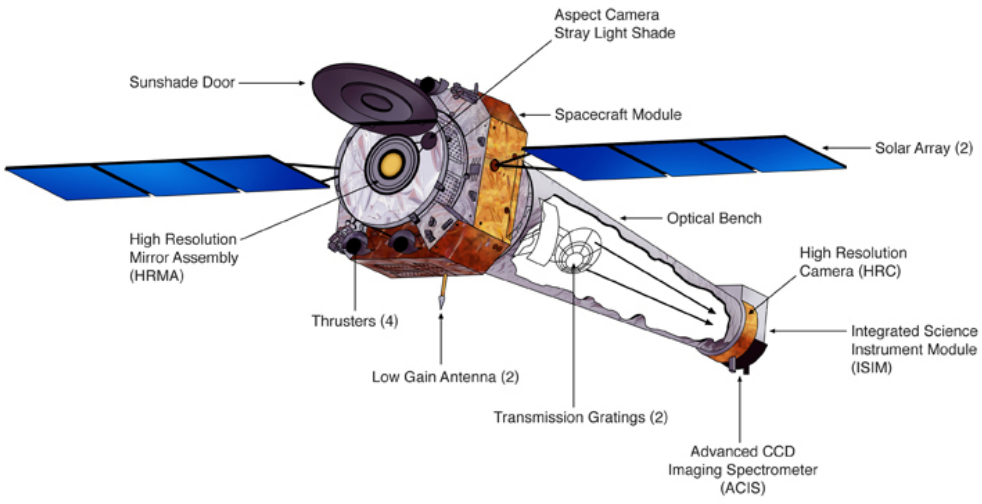

Figure 2.1: Overview of the composition of the Chandra X-ray Observatory. credit: NGST & NASA/CXC

Figure 2.1 gives an overview over the Chandra X-ray observatory, with labels for the most important subsystems. Here the High Resolution Mirror Assembly (HRMA) is of particular interest, since it acts as the focusing optic.
The basis for the type of focusing optic used with Chandra lies in the reflective properties of X-rays. For very smooth surfaces and low incidence angles ($< 1°$)), X-rays do not penetrate the material, but instead are reflected. The efficiency of this reflection is still highly dependent on the photon energy. In Figure 2.2 the reflection efficiency is plotted over the energy for quartz (SiO_2) at 45' and for Gold (Au) and Nickel (Ni) at 30' and 45'.

For low energies the efficiency is approximately 1, while above a certain material and angle dependent energy threshold the efficiency drops considerably. (Seward and Charles (2010)).

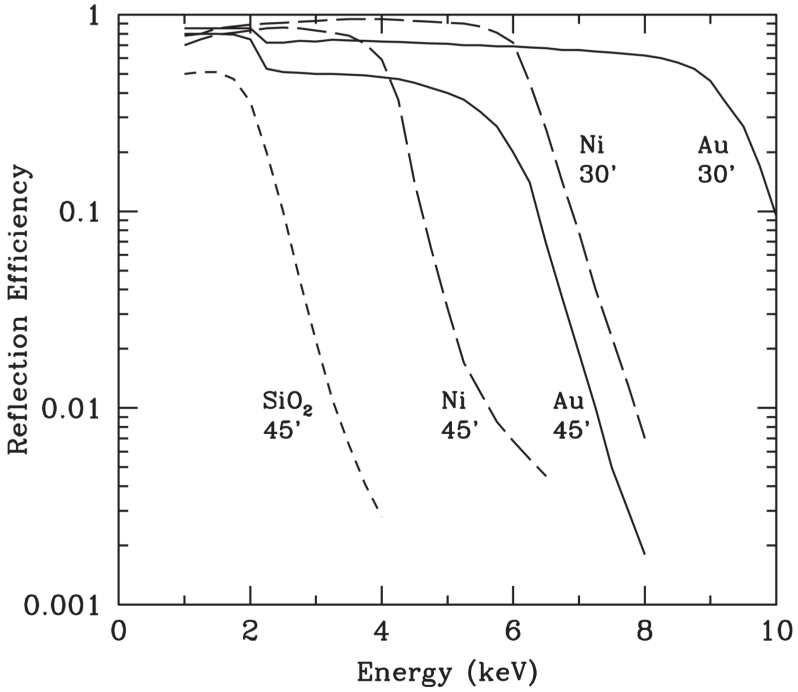

Figure 2.2: X-ray reflection efficiency for different materials at 30 and 45 arcmin. credit: Seward (1977)

Due to the extremely low incidence angles required for the reflection of X-rays, the focusing optic can not use a single large parabolic mirror, as is the case with many optical telescopes. Instead a tube-like assembly of paraboloids and hyperboloids is used, as it was first suggested by Wolter (1952). A schematic of this kind of mirror assembly can be seen in figure 2.3, which depicts the geometry of the mirrors used in the Chandra X-ray Observatory. The incident parallel X-rays are first reflected on the paraboloids, and then on the hyperboloids, to create an image on the focal surface. The nesting of multiple mirrors, as seen in figure 2.3, increases the effective area of the telescope (Seward and Charles (2010)).

An important parameter of telescopes is the Point-Spread-Function (PSF), which describes the surface brightness distribution of a point source image (Seward and Charles (2010)). It is an important factor in regard to the resolution of the telescope.
For Chandra the Full-Width-Half-Maximum (FWHM) of the PSF is $< 0.5''$ in the case of on-axis imaging. With increasing off-axis distance, the PSF broadens (Chandra IPI Teams (2019)).

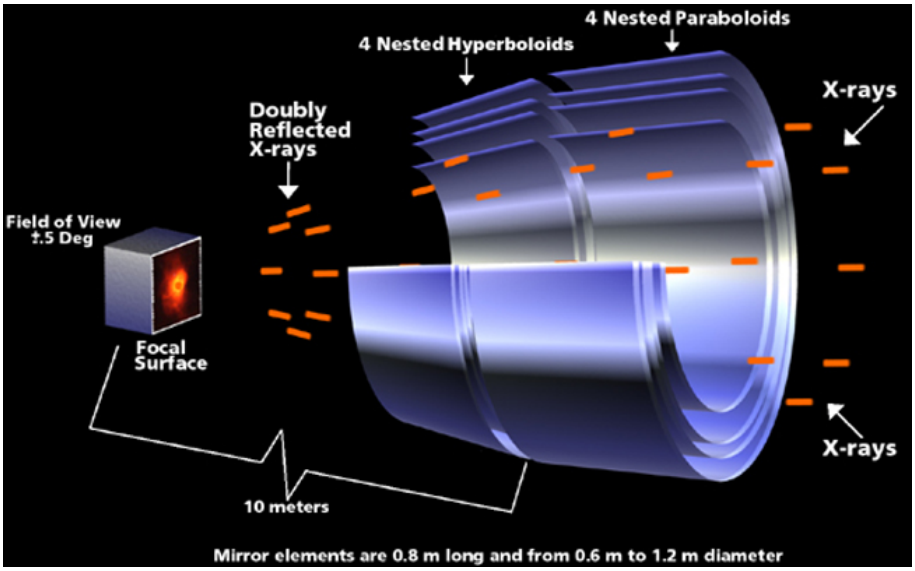

Figure 2.3: A schematic depiction of the mirror assembly used in the Chandra X-ray observatory. The reflection angles are exaggerated for illustrative purposes. credit: NASA/CXC/D.Berry

The centerpiece of Chandra's HRMA consists of the four Iridium coated mirror pairs, assembled in a Wolter Type-I configuration. The telescopes effective areas are 800 cm^2 for 0.25 keV, 400 cm^2 for 5.0 keV and 100 cm^2 for 8.0 keV. The total ghost-free field of view lies at 30' (Chandra IPI Teams (2019)).

Just as important as the High Resolution Mirror Assembly are the two science instruments Chandra carries, the High Resolution Camera (HRC) and the Advanced CCD Imaging Spectrometer (ACIS).
The HRC is comprised of two detectors, the HRC-I used for imaging and the HRC-S which, in conjunction with the Low Energy Transmission Grating (LETG), is used for spectroscopy in the lower energy bands (0.07-0.15 keV).

The ACIS consists of two separate CCD-arrays, the ACIS-I array with 4 CCDs arranged in a 2×2 square and the ACIS-S array with 6 CCDs, arranged in a 1×6 array.
The ACIS can be used for imaging and, using the Low and High Energy Transmission Grating (LETG & HETG), for spectroscopy. Imaging is the main purpose of the ACIS-I array, which offers a $16' \times 16'$ field of view and is comprised of solely front illuminated CCDs. The ACIS-S array, which can be also used for imaging with a $8'\&8'$ field of view, is mainly used for spectroscopy. To this end, the ACIS-S array contains two back illuminated CCDs (S1 & S3), which are more sensitive to lower energies than front illuminated chips, and offer an overall better energy resolution (Chandra IPI Teams (2019))

3 Supernovae

3.1 Introduction

The following introduction is largely based on chapter 75 in the 'Handbook of Supernovae' (see Reynolds (2016)) in conjunction with chapter 8.5 from the book 'Exploring the X-ray Universe' (see Seward and Charles (2010))
Supernovae are one of the most impressive stellar events that are observable. They mark the death of a star with an explosion of barely conceivable magnitude. The energy this explosion injects into it's stars remnant and the surrounding inter-stellar-medium (ISM), about 10^{51} ergs (10^{44} J), is equivalent to the energy our sun will have radiated during it's entire lifetime of about 10 billion years.
While supernovae, happening close enough to be visible with the naked eye are quite rare, occurring once every few centuries, they can offer a spectacular view, some even being visible during the day. Some of these have been historically documented, such as the supernova SN1572, observed by Tycho and Sophie Brahe in the year 1572 (see Figure 3.1).

The last supernova visible with the naked eye occurred during 1987 in the Large-Magellanic-Cloud, named SN1987A. It was the first supernova for which observations of the progenitor star, a B3 supergiant, were available. An additional feature of this event was a coincident neutrino burst, that corroborated theories of the processes involved in a supernova explosion.

Using powerful telescopes, astronomers find hundreds of supernovae with extra-galactic origin every year. These supernovae outside of our galaxy are far too distant to be visible with the naked eye, but they constitute an important tool in astronomy to measure the distance of extra-galactic objects.
Aside from the importance to astronomers, supernovae also play a major role in the galactic life-cycle, enriching the interstellar medium with heavier elements from which new stars and planets are born.
The high energy of supernovae and their remnants, referred to above, makes them of particular interest to X-ray astronomers. In fact, prior to the discovery of cosmic X-ray sources, supernovae and their remnants were the only astronomical objects theoretically predicted to be a source of X-ray emission.

Supernovae can roughly be separated into two basic types, Ia and core collapse, based on the underlying physical mechanism.

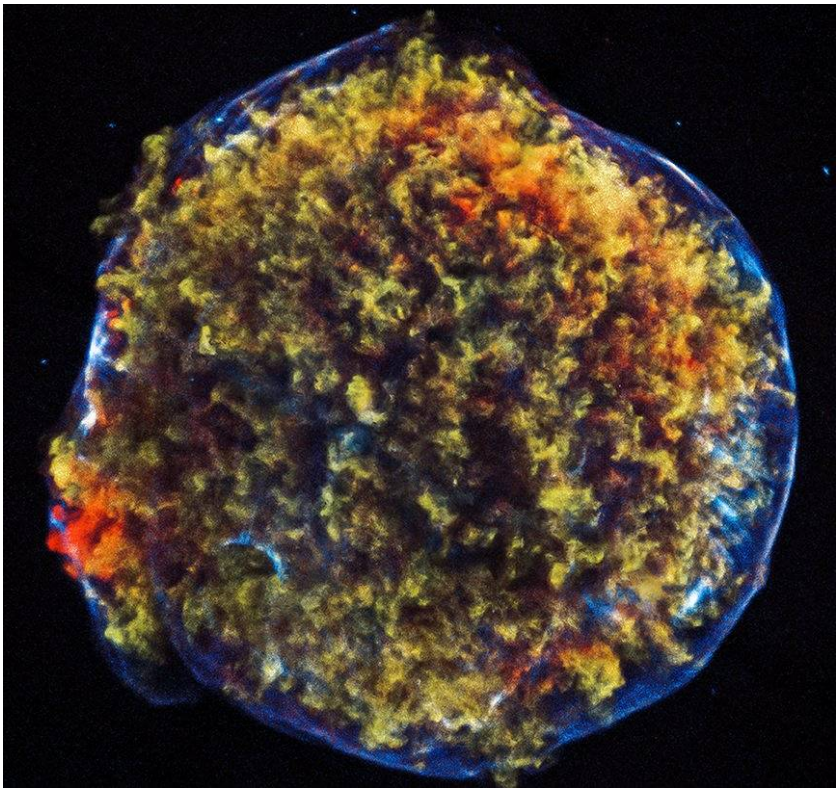

Figure 3.1: X-Ray image of the remnant of the SN1572 supernova, also called Tycho supernova remnant. The image was taken by the Chandra X-Ray observatory and shows a shell of high-energy electrons in blue, and gas heated to millions of degrees Kelvin by the reverse shock in red and green. credit: NASA/CXC/SAO

3.2 Type Ia Supernovae

The energy a star generates is released by nuclear fusion taking place in its core. It is this energy, that stabilizes the star against its own gravitational pull, and prevents it from collapsing in on itself.

In the core, beginning with hydrogen, which is fused into helium, which in turn is fused into carbon and oxygen, heavier elements are formed. A star, that is massive enough, can support fusion up to the element of iron, which has the highest binding energy. Fusion beyond iron would require energy, instead of releasing it, therefore halting further fusion processes.

Stars below 1.44 $M_{\odot}$ (solar masses), the so-called 'Chandrasekhar limit', already cease further fusion when reaching carbon and oxygen. In the absence of stabilizing fusion energy, degenerate electron pressure supports the core to prevent it from collapsing. In a simplified manner, one can imagine the core compressed by gravity to a point, at which the

electrons resist being squeezed together any tighter. These low mass stars do not undergo a supernova-explosion, instead shedding the material around the core in form of a planetary nebula. The remaining, still white-hot core, called a white dwarf, will continue to cool by radiating its heat.

These white dwarfs establish the basis for type Ia supernovae. The starting point is formed by a so-called interacting binary system, with both stars having different, but not too high masses (e.g. 1 $M_\odot$ and 3 $M_\odot$). At first, both stars follow their regular, main sequence evolution, burning hydrogen. The time a star spends doing this is inversely proportional to the square of the stars mass. This means, the more massive primary star evolves first and turns into a giant when it starts to burn hydrogen in the shell around the stellar core. Under normal circumstances this would signify the start of the primary star's red giant phase. If the distance between the two stars is small enough for them to interact, making the system an interacting binary, the outer layers of the giant are either transferred to the smaller secondary star, and/or flung into space.

Through this process, the primary star should have lost enough mass to fall below the aforementioned 'Chandrasekhar-Limit', which means it will develop into a white dwarf and leave the secondary star as the more massive one.
Some time later, the secondary star will also have ceased burning hydrogen and enter its red giant phase. The now expanding secondary star will eventually start to transfer mass from its outer layers to the white dwarf. This mass accretion continues, until the white dwarf's mass reaches the 'Chandrasekhar limit'. At this point, the degenerate electron pressure stabilizing the white dwarf will no longer be able to withstand the gravitational force, and fusion of the white dwarf's carbon and oxygen begins. This sudden onset of thermonuclear burning rips the star apart and causes the type Ia supernova.

Since, according to the described process, the progenitor star of every type Ia supernova is a white dwarf at the 'Chandrasekhar limit', the corresponding explosions should have nearly identical characteristics.
Actual observations have shown that all supernovae of type Ia have very similar light-curves, which not only supports the theoretical model of accreting white dwarfs, but also offers the opportunity to measure the distances of other galaxies.

3.3 Type II Supernovae

Stars above roughly 8 $M_\odot$ show a different behavior, as they continue the diffusion process beyond carbon and oxygen. These massive stars begin their life, just as all other stars, by burning hydrogen in their cores. Differences to lighter stars emerge, as the hydrogen in the core is depleted and helium fusion begins, while hydrogen fusion continues to take place in the layers surrounding the core.

After a life of about ten million years, the star will show an onion-like layer structure with a core devoid of fusion processes, stabilized as a white dwarf by degenerate electron pressure. The core's mass will continuously increase, as fusion products from the surrounding layers sediment additional iron onto it.

Eventually the core will pass the 'Chandrasekhar limit', resulting in a collapse, during which electrons and protons form neutrons and neutrinos, releasing very large amounts of energy. This so-called core-collapse develops within only a few seconds, causing a shock-wave that propagates through the in-falling layers of the dying star, until it reaches and ejects the outer parts into the surrounding space. One is left with a neutron star or even a black hole at the center, and an expanding shell of hot gas, called supernova-remnant. The total energy released during such a core collapse supernova is on the order of 10^{53} ergs, most of which is carried away by the neutrinos.

Core collapse supernovae can have a wide array of progenitor stars with masses between 8 - 25 $M_{\odot}$, which means that their light curves and spectra can vary greatly. Additionally, core collapse supernovae are often further classified, depending on the hydrogen and helium lines in their spectra.
Due to the history of astronomical observations and the resulting classifications, strange naming structures have arisen. Initially type Ia and II supernovae were differentiated by the presence of hydrogen in their optical spectra, with type Ia showing no hydrogen line and type II having a clear hydrogen line. Later observed core collapse supernovae lacked the hydrogen line of the type II supernovae, and were curiously classified as type Ib and Ic where additionally helium was absent.

3.4 Evolution of Supernovae

After a supernova explosion, the ejected material and the shock wave moving into the surrounding circum- or interstellar material, form a structure called supernova remnant. The following section is intended to give an overview of the evolution of these supernova-remnants (SNRs), which can be generally divided into three phases.

The first phase is called the 'ejecta-driven' phase, and can be considered to begin as soon as pressure no longer construes the driving force behind the expansion. The early stage of this phase can be assumed to be a free expansion until approximately a mass equal to that of the ejecta has been swept up. The energy radiated during this phase is insignificant, compared to the kinetic energy unleashed during the supernova explosion, so one can assume an adiabatic expansion.
The supernova blast wave, called forward shock, begins to move into the surrounding circum-stellar material (CSM) or interstellar material (ISM), seeing itself almost instantly decelerated, as it heats the surrounding material to temperatures high enough to emit X-rays. Due to the low densities present, typical values for the ISM are in the range of 1

cm^{-3}, particle collisions are very improbable and shock heating takes place through electromagnetic interactions.

During the swift expansion of a young SNR, the ejecta cools adiabatically to quite low temperatures, meaning even a modest deceleration of the forward shock leads to a supersonic velocity difference in the ejecta. This velocity difference causes a so-called reverse shock, this name being a misnomer at this instance, since the reverse shock at this point also moves outward, albeit at a slower speed than the forward shock.

The forward shock heats up the CSM/ISM as it propagates through it, while the reverse shock is overtaken by cold ejecta, which in turn is heated by the reverse shock. This heated ejecta is separated from the shocked material behind the blast wave by a so-called contact-discontinuity, across which the pressure is more or less constant. A schematic depiction of this 'ejecta-driven' phase can be seen in Figure 3.2. This part of the SNR evolution can last for thousands of years.

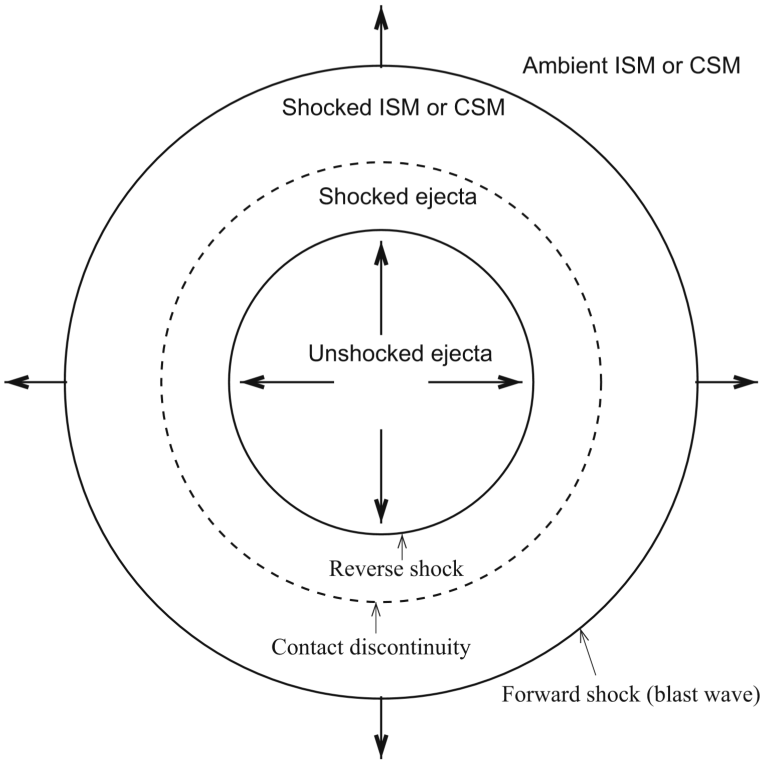

Figure 3.2: Schematic depiction of the ejecta-driven phase. The forward shock propagates into, and heats the surrounding ISM/CSM, while the reverse shock heats up out- flowing cold ejecta. The contact discontinuity in turn separates the hot ejecta from the heated ambient material. credit: (Reynolds, 2016) Figure 1

The structure of the ejecta and shock front depends on the initial composition of the progenitor star and the interaction of the outgoing blast wave with the ambient medium. In general, these conditions are certainly not spherically symmetrical, which in conjunction with the appearance of the surrounding CSM/ISM heavily influences the shape of the SNR. As long as the ejecta overtaking the reverse shock was part of the core surrounding layers, thereby showing a steep incline in density, the reverse shock will move outward. When the central ejecta, with a constant density profile, reaches the reverse shock, it will reverse direction and move inward.

At the point when all the ejecta has been shocked, it can be assumed that the remnant is well in the adiabatic Sedov Phase, being the second phase in the remnant's evolution in this description. In approximation, this occurs once material exceeding ten times the initially ejected mass has been swept up by the shock wave.

To calculate the properties of the SNR in the Sedov phase, again self-similar solutions exist for both a uniform surrounding medium, and a medium expressed through a power-law. The assumption of a uniform medium is in most cases the more effective one. A solution for the outer shock radius in this case is shown by equation 3.1 given by the self-similar solution suggested by Sedov, Neumann and Taylor (Sedov (1959)) A diagram of the velocity, density and pressure profiles derived from self-similar solutions in case of surrounding material with uniform density can be found in Figure 3.3.

$$R_S = 1.15 \cdot \left(\frac{E}{\rho}\right)^{\frac{1}{5}} \cdot t^{\frac{2}{5}} \tag{3.1}$$

When the remnant has reached an age comparable to the time-span required for the heated gas to cool, the radiative phase follows. For general shock speeds of these old remnants, in the range of 200 km s^{-1}, the time scale is found on the order of more than 10000 years. Here, radiated energy is no longer negligible, compared with the kinetic energy, and radiation significantly increases the deceleration of the SNR expansion. If the remnant's center, where cooling proceeds at a much slower rate, offers a high enough density, the shock can still be driven by a 'pressure-driven snowplough'. When even this effect has receded, the SNR material only coasts through the surrounding ISM due to conservation of momentum, until shock speeds fall below the sound-speed of the surrounding medium, and the SNR dissipates.

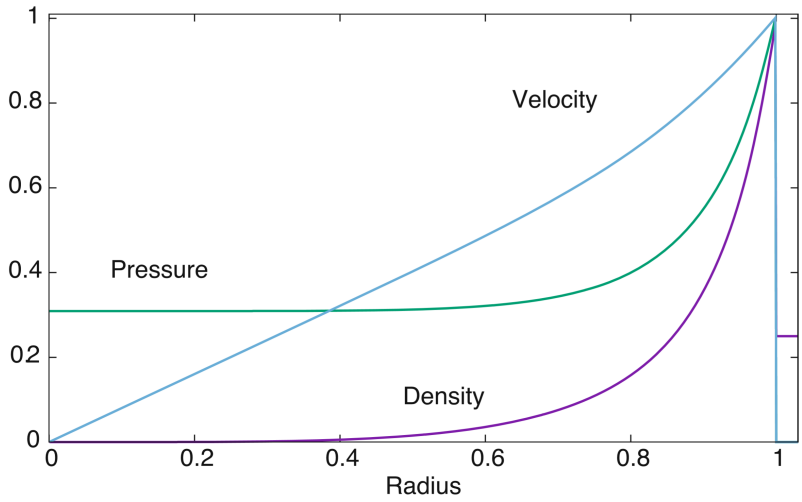

Figure 3.3: Diagram of the velocity, density and pressure profiles in the self-similar Sedov phase for a surrounding material with uniform density. credit: (Reynolds, 2016) Figure 9 top

3.5 X-Ray radiation from supernova remnants

The first X-rays emitted by a supernova originate from a short but powerful burst emitted during the 'shock breakout', when the blast wave initially leaves the star. During the following 'ejecta-driven' and adiabatic stages of the SNR evolution, CSM/ISM heated by the forward shock, as well as ejecta heated by the reverse shock, radiate thermal X-rays. Under the right circumstances, it is possible for non-thermal electrons, accelerated by diffusive shock acceleration, to emit synchrotron radiation even in the X-ray range. In especially young SNRs an additional source of X-rays is provided by radioactive decay of ^{44}Ti into ^{44}Sc which decays into ^{44}Ca.

The thermal X-Ray emission behind the forward shock shows approximately solar abundances, while in the X-ray spectrum behind the reverse shock enhanced abundances of heavier elements are visible. Since in most cases, observations can not spatially separate the forward and reverse shock, distinguishing between the spectral contribution of each poses considerable difficulties.

A further challenge can be found in the under-ionization of the shock heated plasma, since collisional ionization occurs not rapidly enough to establish an immediate equilibrium. This non-equilibrium ionization influences the X-Ray spectrum (e.g. stronger helium-like line emission compared to hydrogen-like) and is quantified by the 'ionization timescale τ' as a measure of the degree of ionization in the plasma. For values of τ considerably larger than 10^{12} cm^{-3} s, it can be assumed that the plasma is in collisional ionization equilibrium.

Arriving at the Sedov phase, the reverse shock reaches the center of the SNR and fades. While X-ray emission from the interior, with enhanced abundances, may still be present, the spectrum is now dominated by the shocked CSM/ISM.

Finally reaching the radiative phase, X-ray emission drastically weakens, leaving optical and radio emission. Since SNRs are very inhomogeneous structures, hot and dense 'clumps' can still persist in older remnants and allow for continued X-Ray emission (e.g. Cygnus Loop).

4 Fundamental Statistics in X-ray Astronomy

4.1 Introduction

The following section is based on the overview given by Siemiginowska (2011).

Statistics are an essential cornerstone in science, forming the basis upon which amongst others, observations, models and even problems themselves are evaluated. X-ray astronomy is no exception and relies heavily on statistics in every step of its research.

One of the main purposes of X-ray analysis lies in describing the physical properties of an observed object. To this end, the data obtained through an observation is compared to a parameterised model. Here, it is attempted to optimize the parameters until the model describes the data in the best possible way. Finding an objective criteria for the 'best way' is one of the difficulties that can only be overcome through the use of statistics. This 'fitting'-process can be divided into three steps:

- defining a model and calculating the optimal parameter values regarding the data.
- obtaining confidence limits of the parameters
- quantifying the quality of the description of the data by the model, called 'goodness-of-fit'.

4.2 Probability distributions

Probability distributions form the beginning of all statistical analyses. It describes the probability for an event to occur under a certain condition (e.g. within a certain interval). For a function $f(x)$ to be a probability distribution, it must fulfill the following requirements:

- $\mathrm{Prob}(a < x < b) = \int_a^b f(x)\mathrm{d}x$
- $\int_{-\infty}^{\infty} f(x)\mathrm{d}x = 1$
- $f(x) \geq 0$ for $x \in \mathbb{R}$

The two most commonly used probability distributions in X-ray astronomy are the Poisson distribution (see eq.4.1) and the Gaussian- or normal distribution (see eq. 4.2).

$$P(n;\mu) = \frac{\mathrm{e}^{-\mu}\mu^n}{n!} \tag{4.1}$$

The Poisson distribution $P(n;\mu)$ is the probability for the occurrence of n events for a given mean value μ. If the measurement is limited to the time t, $P(n;t\mu)$ gives the probability of n events occurring within t.

$$N(n;\mu,\sigma) = \frac{1}{\sigma\sqrt{2\pi}}\exp\left[\frac{-(n-\mu)^2}{2\sigma^2}\right] \tag{4.2}$$

The Gaussian distribution is the probability of n events for a given mean value μ and variance σ^2. Similar to the Poisson distribution, the probability of n events occurring within a time t can be obtained from $N(n;t\mu,t\sigma)$ by multiplying the mean value μ and variance σ with t.
For large mean values μ, the Poisson distribution approaches the Gaussian distribution.

4.3 Model parameter optimization

The selection of models that are chosen for the data analysis is generally based on existing knowledge and theories regarding the source. Each model is comprised of a set of parameters, for which the optimal values that best describe the data have to be determined. To find the best parameter values, the 'likelihood-function', which relates the model to the observed data, is calculated. Equation 4.3 shows the definition of such a likelihood-function, where X_i are the observed data drawn from a probability distribution, Θ represents the model parameters and M_i is the predicted model value for each X_i.

$$\begin{aligned}\mathcal{L}(\{X_i\}) &= \mathcal{L}(X_1, X_2, ..., X_N) \\ &= \mathrm{Prob}(X_1, X_2, ..., X_N \mid \Theta) \\ &= \mathrm{Prob}(X_1 \mid M_1(\Theta))\mathrm{Prob}(X_2 \mid M_2(\Theta))...\mathrm{Prob}(X_N \mid M_N(\Theta)) \\ &= \prod^{N} \mathrm{Prob}(X_i \mid M_i(\Theta))\end{aligned} \tag{4.3}$$

$\mathrm{Prob}(X_i \mid M_i(\Theta))$ shows the probability for a predicted value M_i to be equal to the observed data values X_i. The parameter values of Θ, that maximize the likelihood-function, are called the 'best parameters'.

Should the data result from a Poisson distribution, the likelihood-function can be written as shown in equation 4.4

$$\mathcal{L}(\{X_i\}) = \prod^{N} \mathcal{P}(X_i; M_i(\Theta)) \tag{4.4}$$

In many cases, the logarithm of the likelihood-function (see eq. 4.5) is used to improve calculation efficiency:

$$\ln\mathcal{L} = \sum_{i}^{N} (X_i \ln M_i - M_i - \ln X_i!) \tag{4.5}$$

The term $\ln X_i!$ in equation 4.5 can be disregarded, since it is independent of the model. The Cash statistic as defined in equation 4.6 is obtained through an additional multiplication by -2.

$$C = 2 \sum_{i}^{N} (M_i - X_i \ln M_i) \tag{4.6}$$

A likelihood-function for data from a Gaussian distribution with an independent σ_i can also be derived:

$$\mathcal{L}(\{X_i\}) = \prod^{N} \mathcal{N}(X_i; M_i(\Theta), \sigma_i) \tag{4.7}$$

As with the Poisson-data, a logarithm is applied and the equation is multiplied with -2:

$$-2 \ln\mathcal{L} = \sum_{i}^{N} \frac{(X_i - M_i)^2}{\sigma_i^2} - 2 \sum_{i}^{N} \ln \frac{1}{\sigma\sqrt{2\pi}} \tag{4.8}$$

The second term is not related to the model, and can thus be ignored for the maximization of the likelihood-function. The often used S^2-statistic, also called χ^2-statistic remains:

$$S^2 = \sum_{i}^{N} \frac{(X_i - M_i)^2}{\sigma_i^2} \tag{4.9}$$

4.4 Parameter confidence limits

While C or S^2 can be used to determine the best values for the model parameters, these values also have uncertainties. Just as important as the parameter values themselves, is the information of how accurately the parameters can be ascertained. An important tool for determining this quality of the parameter values is the posterior probability of the model I with the parameter set Θ for the given set of X-ray data $\{X_i\}$:

$$\text{Prob}(\Theta \mid \{X_i\}, I) = \text{Prob}(\{X_i\} \mid \Theta, I)\,\text{Prob}(\Theta \mid I) \tag{4.10}$$

The I stands for the already existing knowledge regarding the source, e.g. the model type, parameter range, distribution of parameters etc. The first term on the right side is the already mentioned likelihood function for the data set $\{X_i\}$ and a model I with parameters Θ. For Poisson- and Gaussian-data respectively, this likelihood function can be found in equations 4.4 and 4.7. The second term on the right side is the prior, i.e., the probability of the model for the given knowledge I.
Normally this equation would require a normalizing factor to warrant that the parameter values lie between 0 and 1.

Since the distribution of the posterior probability from equation 4.10 contains information about every parameter and probability, it can be quite difficult to interpret or understand. To make further analysis more comprehensible, parameter values are given with a confidence region which corresponds to an interval, in which the parameter value lies within a certain probability. To calculate this confidence region, a probability region has to be defined first, e.g. for a 90% probability. After that, all other parameters are integrated, and with the resulting probability distribution, a value range for the parameter of interest is determined for the probability region defined earlier. Finding this value range is certainly not unambiguous, since there are infinite possibilities to choose such a range of values. Most commonly, the smallest range or the range centered on the best parameter value is used.

Another frequently used method to quantify the quality of the calculated fit-parameters is the 'Goodness-of-fit'. Many different statistics exist to calculate the goodness-of-fit value, of which the one given by Pearson F.R.S. (1900) is the most commonly used one:

$$S^2_{\text{Pearson}} = \sum_i^N \frac{(Xi - M_i)^2}{M_i} \tag{4.11}$$

As a general rule of thumb, for a decent fit, the value of S^2_{Pearson} should be close to the number of degrees of freedom. It should be mentioned that this test statistic given by Pearson generally only works for X_i with values ≥ 5.

As a final note regarding statistics in X-ray astronomy, it should be noted that although most data are assumed to origin from a Gaussian distribution, it should in fact be assumed to be of a Poisson distribution. Only for very high count rates, which is not generally the case for X-ray data, a Gaussian distribution can be used as an approximation. The reason for the general use of Gauss statistics, despite the resulting bias, lies mostly within the ease of use, regarding the consideration of the background. Since the difference between two Gaussian distributions is again a Gaussian distribution, the background can easily be subtracted from the data. This is not the case for Poisson distributed data. Hence, a more comprehensive approach to the background has to be taken in this case.

5 Comparison of χ^2 and Cash Statistic fitting using Chandra observational data

As mentioned in the previous chapter, X-ray astronomers often assume a Gaussian distribution for their data, as it simplifies the incorporation of the background data. It was also discussed, that this assumption is, in most cases, quite erroneous, since X-ray data are, except for instances with very high counts, Poisson distributed.
The aim of this chapter is to compare Gaussian statistics (χ^2) and Poisson statistics (Cash Statistic), using observational data from the Chandra X-Ray Observatory. From this data, spectra for different regions will be extracted and fitted with χ^2- and Cash statistic. The comparison of the statistics will then be drawn, based on the results of the fits.

5.1 Data Preparation

The data used originate from Chandra observations of the N19 region in the Small Magellanic Cloud, with the identification numbers 3904, 14674, 15507 and 16367. The observation with ID 3904 was conducted using the ACIS-S array, in particular the back-illuminated S3 chip, while the observations with IDs 14674, 15507 and 16367 were carried out using the entirely front-illuminated ACIS-I array. Before the data preparation could begin, the files from the observations had to be downloaded from the Chandra Data Archive (Smithsonian Astrophysical Observatory (2019)).

The Chandra Interactive Analysis of Observations (CIAO) software package was employed for the data preparation (Fruscione, A., et al. (2006)).
As a first step, the in CIAO contained *chandra_repro* script was used with the data to apply the most current calibration information, creating a new set of event files. Additionally, the energy range of the files was limited to 0.3 keV−10 keV.

Then, using the *dmextract* script, which is also part of CIAO, a light curve was created for every observation which, with the aid of the *lc_clean* script provided Good-Time-Interval (GTI) files, specifying the observation times, without flares, for each observation. These GTI-files were then used to create flare-removed event files for the observations.

After this, exposure maps and Point-Spread-Function (PSF) files were created with the *fluximage* script using a binning value of 4. For this purpose, the energy was separated into three energy ranges: soft (0.5 keV − 1.2 keV), medium (1.2 keV − 2.0 keV) and hard (2.0 keV − 7.0 keV). An exposure map and PSF file was created for each of these energy

ranges and each observation. The PSF files were generated with an energy-conversion-function (ecf) value of 0.393, the default value in the CIAO software, and a value of 0.92 keV for the soft, 1.56 keV for the medium and 3.8 keV for the hard energy band. The energy values for the three different bands are based on definitions from the Chandra Source Catalogue (Chandra X-ray Center (2019)).

The exposure maps and PSF files were then used to detect point sources with the automated *wavdetect* script. This script correlates the image with 'Mexican Hat' wavelets at different scales, given in units of pixels, to detect possible point sources, which are output as a region file. The wavelet scales used were 2.0, 4.0, 8.0 and 16.0 and the script was run separately for every energy band. The resulting three region files were then combined and checked by hand to eliminate false or equivocal detection.

The two regions used for this thesis are the *DEM S32* and *IKT 2* region. An image with the specific regions and point sources used for the analysis can be seen in figure 5.1. The initially separate files for the regions and point sources were then merged to exclude the point sources during the extraction of the spectra.

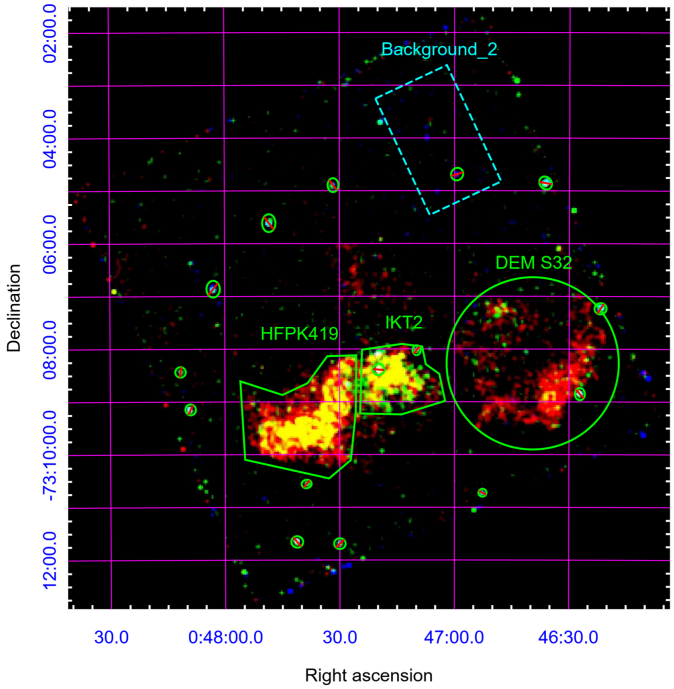

Figure 5.1: Composite RGB-Image of the N19-region with: red (0.5 keV - 1.2 keV), green (1.2 keV - 2.0 keV) and blue (2.0 keV - 7.0 keV). The specific regions considered in this thesis are labeled as DEM S32, IKT2 and HFPK419. Marked out in red, are the point sources that are removed, before the spectra are extracted. The cyan rectangle denotes the background region used for the analysis.

For the last step the actual spectra were extracted from the event files that had been generated with the *chandra_repro* script, using the merged region files containing the point sources.
For that purpose the in CIAO included *specextract* script was used. The script extracts the spectra for the source region, as well as for the background region.
Before the analysis could begin, the *BACKSCAL* value of source and background spectra had to be adjusted. This parameter ensures that the differing size of background and source region is properly taken into account when analyzing the spectra.
The value of *BACKSCAL* was defined as the quotient between the source and background area:

$$BACKSCAL = \frac{Source\ Area}{Background\ Area} \tag{5.1}$$

The source and background area values were determined with the 'ds9fun' software. The calculated *BACKSCAL* value was then entered into the source spectra, while the value in the background spectra was set to 1.

5.2 Comparative Analysis of the Spectral Fits created with Gaussian and Poisson Statistic

In the following section, the fitting results for each region, using χ^2- and Cash statistics will be presented. Fitting was carried out for all ACIS-I observations (14674, 15507, 16367) simultaneously, while the ACIS-S observation (3904) was fitted separately. Two different models were used for each region, one for collisionally ionized diffuse gas (apec), and the other for non-equilibrium ionization collisional plasma (nei). In the case of the apec-model, two separate apec components were assumed. A detailed description of the models can be found in the Xspec user guide (Arnaud K., et al. (2018)).

Since, as already mentioned in previous chapters, a Poisson distribution does not allow for a simple subtraction of the background. The background must also be modelled. The model used for the background can be seen in equation 5.2:

$$constant\langle 1\rangle * [apec\langle 2\rangle + TBabs\langle 3\rangle * (apec\langle 4\rangle + powerlaw\langle 5\rangle) + gaussian\langle 6\rangle] \tag{5.2}$$

List of the different components of the background model in equation 5.2 including the important and all free parameters:

- constant⟨1⟩: scaling factor (free parameter)
- apec⟨2⟩: local bubble emission
  - plasma temperature kT: free parameter
  - normalization: free parameter
- TBabs⟨3⟩: absorption by the Milky Way disk
  - equivalent hydrogen column nH: frozen parameter set to 3×10^{20} $\frac{1}{\mathrm{cm}^2}$
- apec⟨4⟩: galactic halo emission
  - plasma temperature kT: free parameter
  - normalization: free parameter
- power law⟨5⟩: extra galactic X-ray background
  - photon index: frozen parameter set to 1.46
  - normalization: free parameter
- gaussian⟨6⟩: Si-peak originating from detector
  - line energy: free parameter
  - sigma: frozen parameter set to 0

A detailed description of all models used for the background can be found in the Xspec user guide (Arnaud K., et al. (2018)).

5.2.1 Fit results of the DEM S32 region

This section presents the results of the spectral fits for the DEM S32 region (see fig. 5.1). Two different models from the Xspec software were used for the fits, a non-equilibrium ionization collisional plasma model (vnei) and an emission spectrum from collisionally-ionized diffuse gas (vapec) (Arnaud K., et al. (2019)). In the case of the vapec-model, two separate components were fitted simultaneously.

The parameters for the models are as follows:

- vnei:
  - plasma temperature kT [keV]
  - elemental abundances for H, He, C, N, O, Ne, Mg, Si, S, Ar, Ca, Fe and Ni with respect to to the solar values
  - ionization timescale τ $[\frac{s}{cm^3}]$
  - redshift z
  - normalization (norm.)
- vapec:
  - plasma temperature kT [keV]
  - elemental abundances for He, C, N, O, Ne, Mg,Al, Si, S, Ar, Ca, Fe and Ni with respect to the solar values
  - redshift z
  - normalization (norm.)

Not all model parameters are free parameters for the purpose of this analysis, in fact most are set to known or assumed values, originating from previous knowledge. The abundances for H and He are assumed to be of solar value, and are set to 1 for all fits. Also fixed across all spectra is the redshift, which is presumed to be negligible and set to 0. The abundances of the metals in each model are set to 0.2, the value for the SMC. Most are fixed, while, depending on the actual model and spectra fitted, some values are set as free parameters. The parameters that are not fixed to certain values are then used in the calculation of the fit, as described in chapter 3.3. In the results presented, each parameter is given with its best-fit value, as well as the 90% confidence range for this parameter.

The first fits were performed for the DEM S32 region using the ACIS-S observation (obs. ID 3904). The fit results for the vnei-model, calculated with Gaussian χ^2-statistic can be seen in figure 5.2. The results for the calculation with Poisson C-statistic are shown in figure 5.3.

Free parameters for this case were the plasma temperature (kT), the abundances of Mg and Si, the ionization timescale (τ) and the normalization. The resulting parameter values for the χ^2-statistic are shown in table 5.1 with the corresponding 90% confidence range. For the C-statistic calculation, the resulting parameter values can be found in table 5.2.

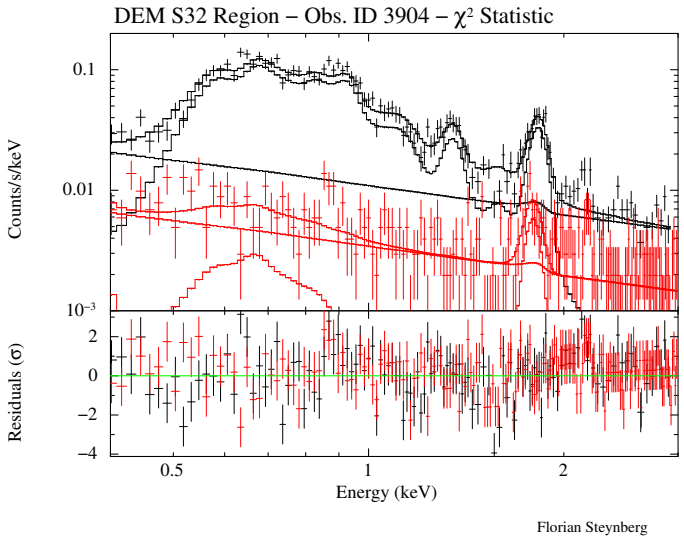

Figure 5.2: Spectral fit for the DEM S32 Region with with the vnei model and Gaussian statistic using the ACIS-S observation (Obs. ID 3904). The bottom plot shows the residuals in terms of σ with error-bars of 1σ.

Parameter	min. value	best-fit value	max. value
kT [keV]	0.5164	0.588172	0.698427
Mg	0.309314	0.420601	0.542082
Si	2.9569	3.99239	5.30769
τ $\left[\frac{\mathrm{s}}{\mathrm{cm}^3}\right]$	8.51267×10^9	1.08089×10^{10}	1.36501×10^{10}
norm.	3.03289×10^{-4}	3.53290×10^{-4}	4.00497×10^{-4}

Table 5.1: Parameter values for the spectral fit of the DEM S32 region with the vnei model and Gaussian statistic using the ACIS-S observation (Obs. ID 3904). The minimum and maximum values give the 90% confidence range for the parameter.

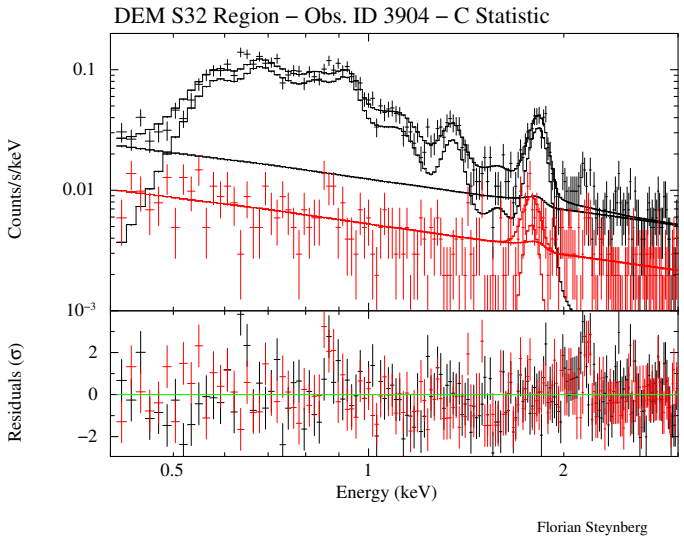

Figure 5.3: Spectral fit for the DEM S32 Region with with the vnei model and Poisson statistic using the ACIS-S observation (Obs. ID 3904). The bottom plot shows the residuals in terms of σ with error-bars of 1σ.

Parameter	min. value	best-fit value	max. value
kT [keV]	0.423723	0.477238	0.556838
Mg	0.30689	0.414586	0.53697
Si	4.20372	5.55163	7.53562
τ $\left[\frac{s}{cm^3}\right]$	9.87866×10^{9}	1.28007×10^{10}	1.65294×10^{10}
norm.	4.68647×10^{-4}	5.58486×10^{-4}	6.46182×10^{-4}

Table 5.2: Parameter values for the spectral fit of the DEM S32 region with the vnei model and Poisson statistic, using the ACIS-S observation (Obs. ID 3904). The minimum and maximum values give the 90% confidence range for the parameter.

The Gaussian fit was conducted with 287 Degrees of Freedom (DoF) resulting in a reduced χ^2 of 1.3206, while the Poisson fit ran with 337 DoF and a reduced χ^2 of 1.7300.
The reduced χ^2 can only be used as a very rough indication of the fit quality, since the statistic of the background shows zero variance in some energy bins due to the low count rates. Furthermore, the reduced χ^2 is not actually applicable to Poisson distributed data, but since both fits are expected to be similar, it can be used for comparative purposes.

A visual comparison of the two plots (fig. 5.2 & 5.3) shows only very little difference between the fit using χ^2-statistics and the fit using Cash statistic. A comparison of the fit parameters from table 5.1 and 5.2 shows that the values for all parameters are on the same order of magnitude. A difference between the parameter values is to be expected,

since the Gaussian fit for actually Poisson distributed data introduces a bias. A look at the confidence intervals shows further, that all best-fit values of each parameter lie within the limits of both fits.

The fit results using two vapec-models for the DEM S32 region can be found in figure 5.4 and 5.5 as well as tables 5.3 and 5.4.

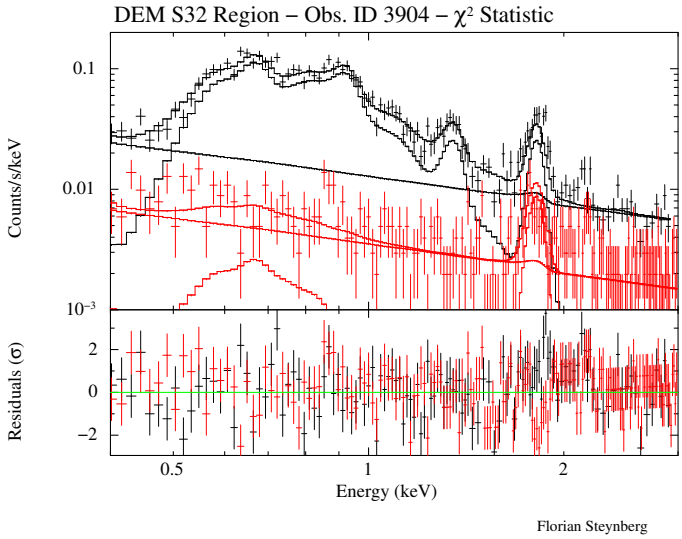

Figure 5.4: Spectral fit for the DEM S32 Region with with two vapec-models and Gaussian statistic using the ACIS-S observation (Obs. ID 3904). The bottom plot shows the residuals in terms of σ with error-bars of 1σ.

Parameter	min. value	best-fit value	max. value
kT (vapec1) [keV]	0.163527	0.173734	0.178521
Mg (vapec1)	0.729533	1.00935	1.34407
norm (vapec1)	6.85452×10^{-3}	7.59305×10^{-3}	8.99852×10^{-3}
kT (vapec2) [keV]	0.63965	0.810729	1.04667
norm. (vapec2)	5.0507×10^{-5}	8.93767×10^{-5}	1.39482×10^{-4}

Table 5.3: Parameter values for the spectral fit of the DEM S32 region with 2 vapec models and Gaussian statistic using the ACIS-S observation (Obs. ID 3904). The minimum and maximum values give the 90% confidence range for the parameter.

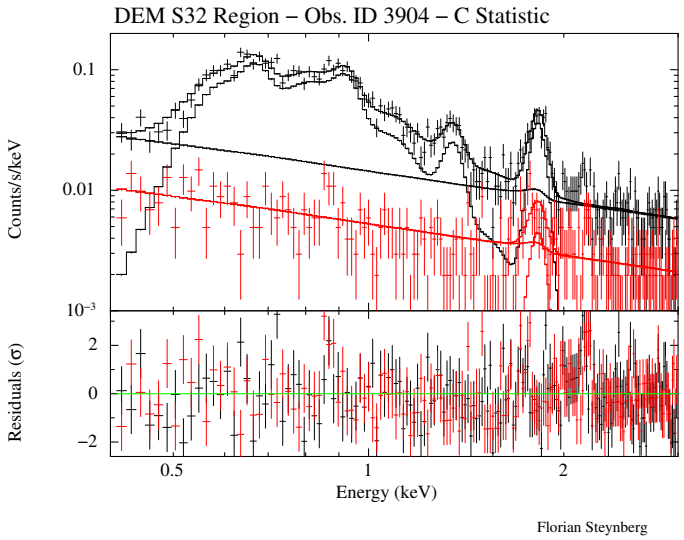

Figure 5.5: Spectral fit for the DEM S32 Region with with two vapec-models and Poisson statistic using the ACIS-S observation (Obs. ID 3904). The bottom plot shows the residuals in terms of σ with error-bars of 1σ.

Parameter	min. value	best-fit value	max. value
kT (vapec1) [keV]	0.158131	0.173458	0.177124
Mg (vapec1)	0.627912	0.841888	1.1324
norm (vapec1)	9.32843×10^{-3}	1.03110×10^{-2}	1.34409×10^{-2}
kT (vapec2) [keV]	0.231195	0.990389	n.a.
norm. (vapec2)	4.34548×10^{-6}	3.0247×10^{-5}	6.37245×10^{-4}

Table 5.4: Parameter values for the spectral fit of the DEM S32 region with two vapec-models and Poisson statistic using the ACIS-S observation (Obs. ID 3904). The minimum and maximum values give the 90% confidence range for the parameter. The upper limit of the plasma temperature confidence range for the second vapec-model is not available, since it ran into its upper limit during the calculation.

For these fits, the free parameters were the plasma temperature (kT) and normalization for both vapec-models, as well as the abundance of Mg for the first vapec-model.

The Gaussian fit was conducted with 297 DoF and a reduced χ^2 of 1.3983, while the Poisson fit had 337 DoF resulting in a reduced χ^2 of 1.7371. The same limitations to the reduced χ^2, as with the vnei-model, also apply here.

Visually the two fits for the vapec-model show a stronger deviation in their plots (fig. 5.4 & 5.4) than the ones for the vnei-model, especially at the strong peak to the far right.

The best-fit parameter values found in table 5.3 and 5.4 again find themselves on the same order of magnitude. For the plasma temperature of the second vapec-model no upper limit of the confidence range can be given, since during the calculation, it reached the maximum value possible.

For the fits with the two models, vnei and two vapec, the use of Cash statistic seem to deliver plausible results. Plasma temperatures as well as abundances, all lie within the confidence intervals of either fit statistic. This is supported by the appearance of the plots, that show no major deviations from one another. The Cash statistic fit for the two vapec models offered some difficulties when calculating the confidence limits.

The four fits described in this section were also conducted for the ACIS-I observations (Obs. IDs 14674, 15507, 16367), one for each model (vnei, 2 vapec) and statistic (χ^2 & Cash). The ACIS-I observations suffer from worse statistics compared to the ACIS-S observation resulting in a more difficult fit process. Especially the background proved to be problematic, containing many energy bins with no variance, making the background model unreliable.

The fitting results for the ACIS-I observations can be found in the Appendix, with the plots being shown in figures 1 through 4, and the fitting parameters displayed in tables 1 through 4.
Table 5.5 lists the Degrees of Freedom as well as the reduced χ^2 for the ACIS-I fits:

Fit	Degrees of Freedom	reduced χ^2
vnei (Gaussian)	680	0.60954
vnei (Poisson)	1087	1.02909
2 vapec (Gaussian)	680	0.65264
2 vapec (Poisson)	1087	1.04037

Table 5.5: Degrees of Freedom and reduced χ^2 values for the fits conducted with the ACIS-I data. A fit was calculated using each model (vnei & 2 vapec) and statistic (χ^2 & Cash). The plots and parameter values can be found in the Appendix, figures 1 through 4 and tables 1 through 4

While the reduced χ^2 may initially imply good fit results, the extremely low statistics cause many zero variance bins in the background, introducing a heavy bias. Although this problem exists for the ACIS-S as well as for the ACIS-I data, it is more prominent in the ACIS-I data.

5.2.2 Fit results of the IKT2 region

In this section the fitting results for the spectra of the IKT2 region (see fig. 5.1) are presented. The ACIS-S data are, as with the DEM S32 region, fitted with a model consisting of two vapec components and a vnei model. The ACIS-I data on the other hand are fitted with a single model consisting of only one vapec component. The parameters of each model component (vnei & vapec) are the same as in the previous section.

The plots for the fits with the vnei model can be found in figure 5.6 for Gaussian statistic and figure 5.7 for Poisson statistic.
Tables 5.6 and 5.7 list the fit parameter values for the vnei fits of the IKT2 region. Each value is given with its best-fit value as well as the 90% confidence region.

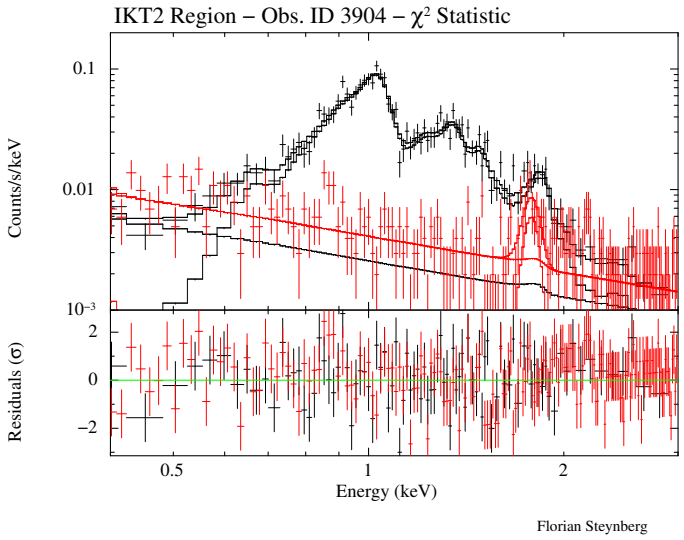

Figure 5.6: Spectral fit for the IKT2 region with with the vnei model and Gaussian statistic using the ACIS-S observation (Obs. ID 3904). The bottom plot shows the residuals in terms of σ with error-bars of 1σ.

Parameter	min. value	best-fit value	max. value
kT [keV]	0.842	0.993410	1.299
O	0.420249	1.43056	2.60179
Ne	0.957055	2.02136	5.79583
Mg	0.687935	1.11702	1.94571
Si	0.32	0.561677	0.968
τ $[\frac{s}{cm^3}]$	9.11735×10^{10}	2.01284×10^{11}	4.59126×10^{11}
norm.	9.88×10^{-5}	1.26202×10^{-4}	1.53×10^{-4}

Table 5.6: Parameter values for the spectral fit of the IKT2 region with the vnei model and Gaussian statistic using the ACIS-S observation (Obs. ID 3904). The minimum and maximum values give the 90% confidence range for the parameter.

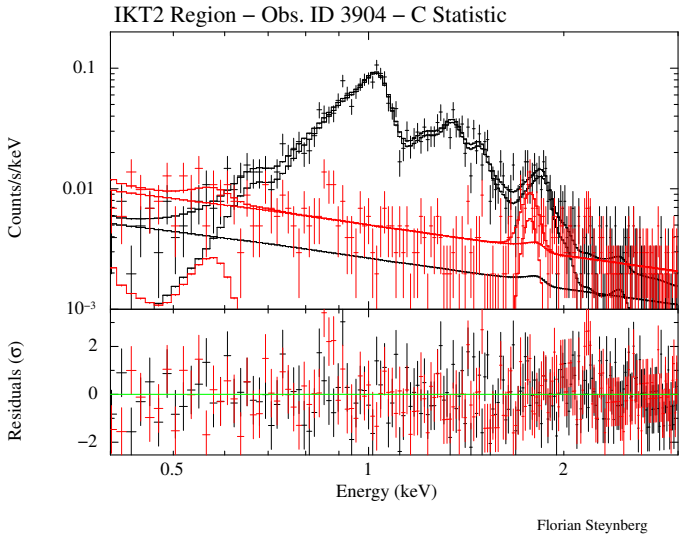

Figure 5.7: Spectral fit for the IKT2 region with with the vnei model and Poisson statistic using the ACIS-S observation (Obs. ID 3904). The bottom plot shows the residuals in terms of σ with error-bars of 1σ.

The free parameters for these vnei fits were the plasma temperature (kT), the ionization timescale (τ), the normalization and the abundances of O, Ne, Mg and Si.
The Gaussian fit was conducted with 260 Degrees of Freedom (DoF) resulting in a reduced χ^2 of 1.1758. The Poisson fit used 349 DoF yielding a reduced χ^2 of 1.4139.
As was the case with the fits in the previous chapter, the reduced χ^2 suffers from the low statistics, causing bins with zero variance and from the fact, that it is only valid as an approximation for Poisson distributed data.

Parameter	min. value	best-fit value	max. value
kT [keV]	0.833	0.975838	1.2
O	0.453056	1.23454	2.21398
Ne	1.01096	2.07813	5.61755
Mg	0.761614	1.20485	2.05616
Si	0.325169	0.561984	0.961518
τ $[\frac{s}{cm^3}]$	1.11415×10^{11}	2.17928×10^{11}	4.62105×10^{11}
norm.	1.01992×10^{-4}	1.29579×10^{-4}	1.5680×10^{-4}

Table 5.7: Parameter values for the spectral fit of the IKT2 region with the vnei model and Poisson statistic using the ACIS-S observation (Obs. ID 3904). The minimum and maximum values give the 90% confidence range for the parameter.

A visual inspection of the plots in figure 5.6 and 5.7, again shows no meaningful deviation in the fits of the source data. The parameter values from table 5.6 and 5.7 not only lie on the same order of magnitude, but show very little deviation at all. As with the previous fits all best-fit values lie in their own and in the confidence interval of the other statistic.

The plots of the fits, for the model consisting of two vapec components, are shown in figures 5.8 and 5.9 with the corresponding parameter values listed in tables 5.8 and 5.9.

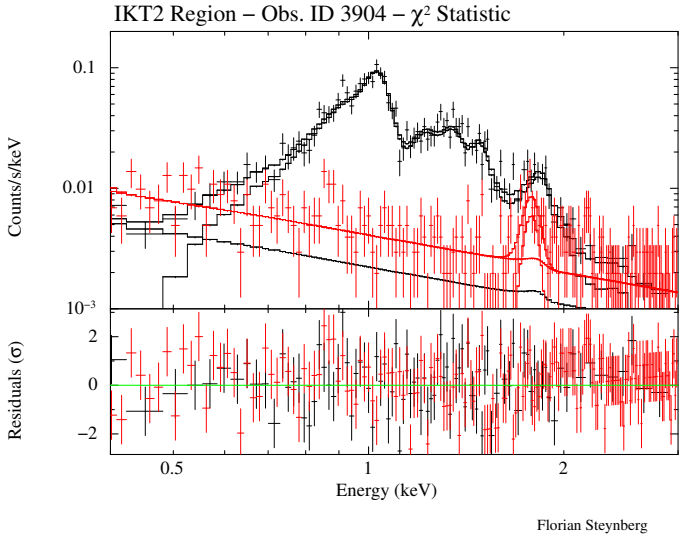

Figure 5.8: Spectral fit for the IKT2 region with with the 2 vapec model and Gaussian statistic using the ACIS-S observation (Obs. ID 3904). The bottom plot shows the residuals in terms of σ with error-bars of 1σ.

Parameter	min. value	best-fit value	max. value
kT (vapec1) [keV]	0.110033	0.153171	0.193293
norm. (vapec1)	3.05542×10^{-4}	7.34131×10^{-4}	2.62154×10^{-3}
kT (vapec2) [keV]	0.701596	0.778080	0.856261
Ne (vapec2)	5.73434	7.60270	10.3543
Mg (vapec2)	1.50086	1.11722	2.97017
Si (vapec2)	0.41348	0.744902	1.23284
norm. (vapec2)	1.10827×10^{-4}	1.45485×10^{-4}	1.81797×10^{-4}

Table 5.8: Parameter values for the spectral fit of the IKT2 region with the 2 vapec model and Gaussian statistic using the ACIS-S observation (Obs. ID 3904). The minimum and maximum values give the 90% confidence range for the parameter.

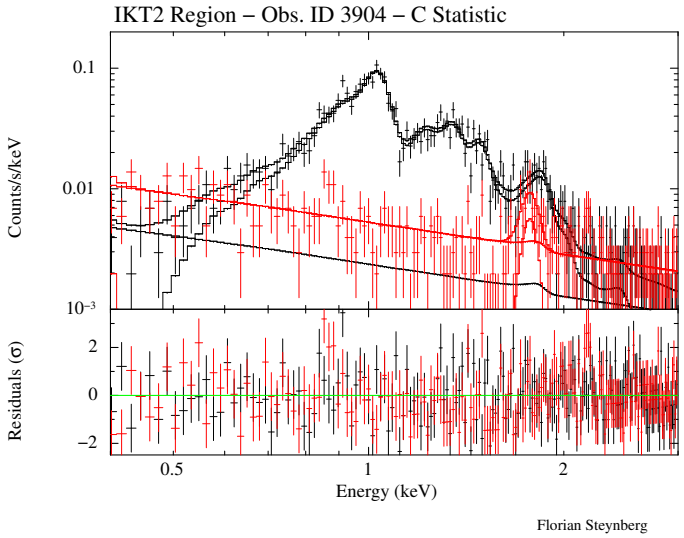

Figure 5.9: Spectral fit for the IKT2 region with with the 2 vapec model and Poisson statistic using the ACIS-S observation (Obs. ID 3904). The bottom plot shows the residuals in terms of σ with error-bars of 1σ.

The free parameter of these fits with two vapec components, were the plasma temperature (kT) and normalization for both vapec components, as well as the abundance of Ne, Mg and SI for one vapec-model (first for Cash statistic, second for χ^2-statistic).

The Gaussian fit for the vapec model was conducted with 260 DoF and a reduced χ^2 of 1.1800. For the Poisson fit 349 DoF were used resulting in a reduced χ^2 of 1.4475.
As with all previous fits, the reduced χ^2 is limited in its reliability, but it implies, with being close to 1, that there are no grave deviations in the fit. A visual comparison of the plots (fig. 5.8 & 5.9) corroborates this implication by not showing any notable deviations.

Parameter	min. value	best-fit value	max. value
kT (vapec2) [keV]	0.113116	0.149446	0.18751
norm. (vapec2)	7.14592×10^{-4}	1.68283×10^{-3}	5.39318×10^{-3}
kT (vapec1) [keV]	0.637371	0.745467	0.816268
Ne (vapec1)	5.1047	6.84878	9.67569
Mg (vapec1)	1.35496	1.86770	2.65253
Si (vapec1)	0.344319	0.621266	1.04582
norm. (vapec1)	1.31306×10^{-4}	1.76047×10^{-4}	2.20112×10^{-4}

Table 5.9: Parameter values for the spectral fit of the IKT2 region with the 2 vapec model and Poisson statistic using the ACIS-S observation (Obs. ID 3904). The minimum and maximum values give the 90% confidence range for the parameter. The two vapec components switch their role compared to the Gaussian fit. This poses no problem, since both vapec components are initialized with identical parameter values. It is still the warmer vapec component that contains the elemental abundances as free parameters.

A look at the parameters listed in tables 5.8 and 5.9, shows very similar values, with all best-fit values of one statistic lying in the 90% confidence region of the other statistic.

The fits for ACIS-I data (Obs. IDs 14674, 15507, 16367) turned out to be problematic. Neither a vnei model, nor the model with two vapec components supplied reasonable parameter values. In the end a model with a single vapec component could be fitted with sensible and relatively stable fit values. The results of the two fits, Gaussian and Poisson, for this single vapec model can found in the Appendix as figures 5 and 6 and as tables 5 and 6.
The Gaussian fit for the single vapec model had 623 DoF and reduced χ^2 of 0.57375. The Poisson fit used 1088 DoF, resulting in a reduced χ^2 of 0.66904.
As with the ACIS-I data from the DEM S32 region, the fits suffer from the low statistics, which especially affects the background.

6 Conclusion and Outlook

The aim of this thesis was the comparison between Gaussian (here χ^2) statistics and Poisson (here Cash) statistics in the analysis of X-ray spectral data. The data used originated from two regions in the N19 region which is located in the Small Magellanic Cloud. Data from Chandras ACIS-S array as well as the ACIS-I array was used.
The ACIS-I data provided very low statistics compared to the ACIS-S data, resulting in ambiguous and unstable fits. The ACIS-S data, more suited for spectral analysis, resulted in clearer and more stable fit results.

The main difference in using Poisson statistics instead of Gaussian statistics lies in the requirement of incorporating a background model. In the scope of this work the background, both the χ^2- and Cash statistics used the same background model to compare the two methods on equal grounds.

The fits for both regions, DEM S32 and IKT2, show no major deviations between the fits using Gaussian or Poisson statistic (see Capter 5.2.1 & 5.2.2). Neither the plots nor the parameter values show large differences, which would indicate a fundamental impediment using Poisson statistics.
The source regions used in this thesis offered relatively low statistics, especially in the case of the ACIS-I data. Data with stronger statistics should show the expected bias more clearly

The main obstacle arising from the use of Poisson statistics compared to Gaussian statistics is the requirement for a background model, which introduces additional parameters, subsequently increasing the difficulty and computation time of the fit.
To define such a background model profound knowledge about the background present at the observed source region is necessary.

In the case of extended sources it may not be advisable to simply subtract the background even when using Gaussian statistics. In these instances the use of Poisson statistics offers no disadvantages compared to Gaussian statistics.

In conclusion it can be reasoned that, the use of Poisson statistics may introduce additional obstacles into the fitting process, but that sound results are given.

In the scope of this thesis only a single background model was used for all fits. Since dealing with the background is not trivial for Poisson statistics, future pursuits in this field

of investigation should focus more intensively on the background model. In addition the data used, should possibly originate from a better known and understood source to further examine the bias introduced by using Gaussian instead of Poisson statistics.

Bibliography

Arnaud K., et al. (2018). Users' Guide for version 12.10.1. https://heasarc.gsfc.nasa.gov/docs/xanadu/xspec/manual/XspecManual.html. [Online; accessed 30-December-2019].

Arnaud K., et al. (2019). Xspec - An X-Ray Spectral Fitting Package. https://heasarc.gsfc.nasa.gov/docs/xanadu/xspec/index.html. [Online; accessed 23-December-2019].

Chandra IPI Teams (2019). The Chandra Proposers' Observatory Guide. http://cxc.harvard.edu/proposer/POG/html/index.html. [Online; accessed 30-December-2019].

Chandra X-ray Center (2019). Chandra Source Catalog Release 2.0 (CSC 2.0). https://cxc.harvard.edu/csc2/. [Online; accessed 30-December-2019].

Fruscione, A., et al. (2006). Chandra Interactive Analysis of Observations (CIAO). https://cxc.cfa.harvard.edu/ciao/. [Online; accessed 16-December-2019].

Giacconi, R., Gursky, H., Paolini, F. R., and Rossi, B. B. (1962). Evidence for x Rays From Sources Outside the Solar System. , 9(11):439–443.

Pearson F.R.S., K. (1900). X. on the criterion that a given system of deviations from the probable in the case of a correlated system of variables is such that it can be reasonably supposed to have arisen from random sampling. *The London, Edinburgh, and Dublin Philosophical Magazine and Journal of Science*, 50(302):157–175.

Reynolds, S. P. (2016). *Dynamical Evolution and Radiative Processes of Supernova Remnants*, pages 1–24. Springer International Publishing, Cham.

Sedov, L. I. (1959). *Similarity and Dimensional Methods in Mechanics*.

Seward, F. (1977). Reflection efficiencies of x-ray mirrors 1-10 kev.

Seward, F. D. and Charles, P. A. (2010). *Exploring the X-ray Universe*. Cambridge University Press, 2 edition.

Siemiginowska, A. (2011). *Statistics*, page 131–145. Cambridge Observing Handbooks for Research Astronomers. Cambridge University Press.

Smithsonian Astrophysical Observatory (2019). Chandra Data Archive (CDA) in the The Chandra X-Ray Center (CXC). https://cxc.cfa.harvard.edu/cda/. [Online; accessed 16-December-2019].

WKT (2002). Major Milestones In X-ray Astronomy. https://chandra.harvard.edu/chronicle/0202/40years/index.html. [Online; accessed 30-December-2019].

Wolter, H. (1952). Spiegelsysteme streifenden Einfalls als abbildende Optiken für Röntgenstrahlen. *Annalen der Physik*, 445(1):94–114.

Appendix

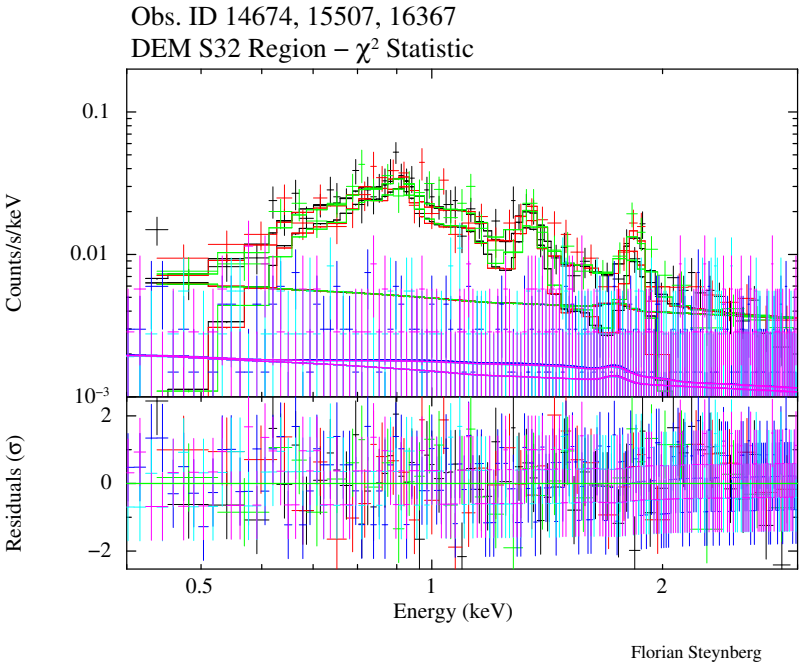

Figure 1: Spectral fit for the DEM S32 Region with with the vnei model and Gaussian statistic using the ACIS-I observations (Obs. IDs 14674, 15507, 16367). The bottom plot shows the residuals in terms of σ with error-bars of 1σ.

Parameter	min. value	best-fit value	max. value
kT [keV]	0.371786	0.450457	0.553784
Mg	0.3458	0.480340	0.0.6346
Si	2.02344	3.29070	5.2505
τ $[\frac{s}{cm^3}]$	1.16878×10^10	1.69859×10^{10}	3.23836×10^{10}
norm.	3.87922×10^{-4}	5.50720×10^{-4}	7.99428×10^{-4}

Table 1: Parameter values for the spectral fit of the DEM S32 region with the vnei model and Gaussian statistic using the ACIS-I observations (Obs. IDs 14674, 15507, 16367). The minimum and maximum values give the 90% confidence range for the parameter.

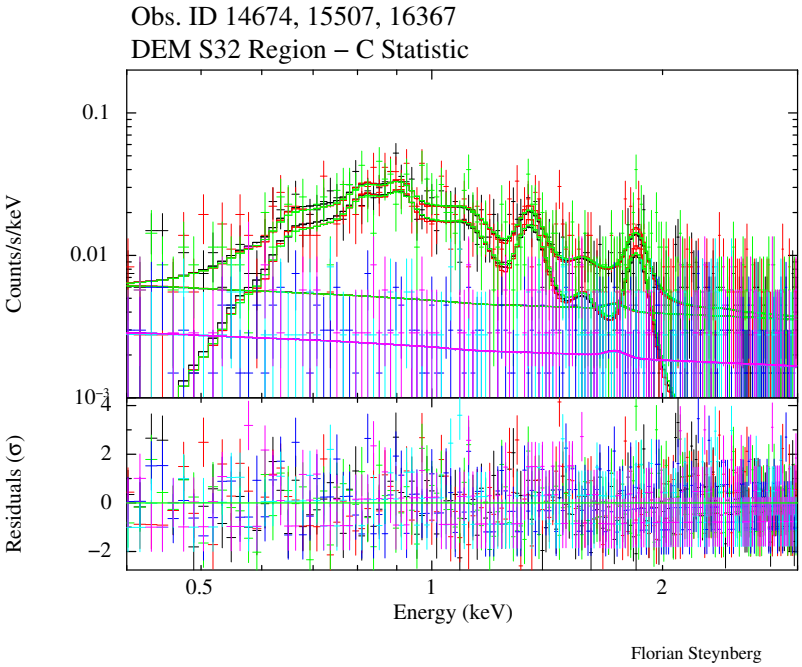

Figure 2: Spectral fit for the DEM S32 Region with with the vnei model and Poisson statistic using the ACIS-I observations (Obs. IDs 14674, 15507, 16367). The bottom plot shows the residuals in terms of σ with error-bars of 1σ.

Parameter	min. value	best-fit value	max. value
kT [keV]	0.5125	0.840245	0.854
Mg	0.308	0.396988	0.559
Si	0.388	0.777619	1.1075
τ $[\frac{\mathrm{s}}{\mathrm{cm}^3}]$	8.75×10^9	1.15796×10^{10}	8.6×10^{10}
norm.	1.675×10^{-4}	1.86259×10^{-4}	3.025×10^{-4}

Table 2: Parameter values for the spectral fit of the DEM S32 region with the vnei model and Poisson statistic using the ACIS-I observations (Obs. IDs 14674, 15507, 16367). The minimum and maximum values give the 90% confidence range for the parameter.

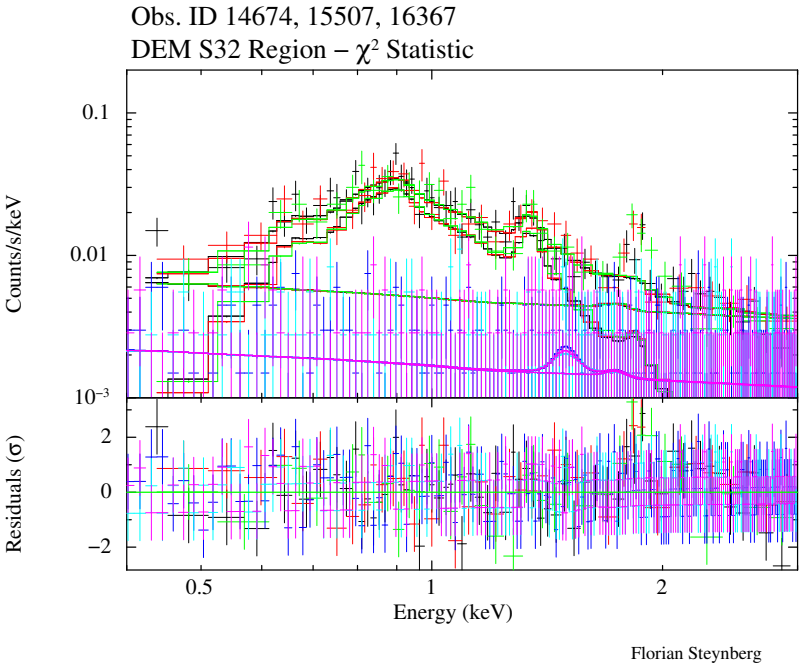

Figure 3: Spectral fit for the DEM S32 Region with with two vapec-models and Gaussian statistic using the ACIS-I observations (Obs. IDs 14674, 15507, 16367). The bottom plot shows the residuals in terms of σ with error-bars of 1σ.

Parameter	min. value	best-fit value	max. value
kT (vapec1) [keV]	0.147298	0.173636	0.209201
Mg (vapec1)	1.03673	1.97485	3.1394
norm (vapec1)	1.53374×10^{-3}	2.74072×10^{-3}	4.87721×10^{-3}
kT (vapec2) [keV]	0.596094	0.686284	0.814227
norm. (vapec2)	1.30844×10^{-4}	2.04987×10^{-4}	2.62353×10^{-4}

Table 3: Parameter values for the spectral fit of the DEM S32 region with 2 vapec models and Gaussian statistic using the ACIS-I observations (Obs. IDs 14674, 15507, 16367). The minimum and maximum values give the 90% confidence range for the parameter.

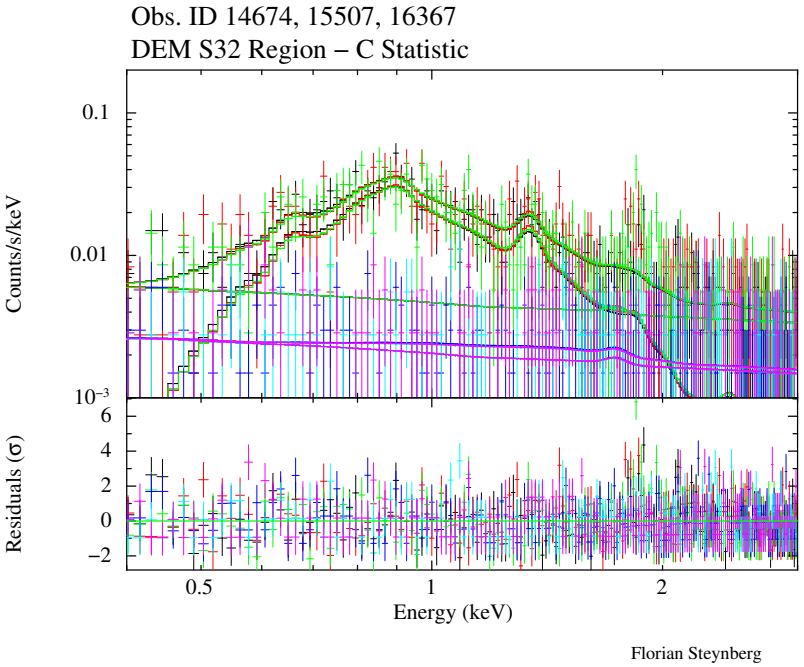

Figure 4: Spectral fit for the DEM S32 Region with with two vapec-models and Poisson statistic using the ACIS-I observations (Obs. IDs 14674, 15507, 16367). The bottom plot shows the residuals in terms of σ with error-bars of 1σ.

Parameter	min. value	best-fit value	max. value
kT (vapec1) [keV]	0.1535	0.179846	0.219
Mg (vapec1)	0.82	1.65795	3.09
norm (vapec1)	1.0592×10^{-3}	1.85540×10^{-3}	3.007×10^{-3}
kT (vapec2) [keV]	0.614486	0.702171	0.851068
norm. (vapec2)	1.13002×10^{-4}	1.78143×10^{-4}	2.3331×10^{-4}

Table 4: Parameter values for the spectral fit of the DEM S32 region with two vapec-models and Poisson statistic using the ACIS-I observations (Obs. IDs 14674, 15507, 16367). The minimum and maximum values give the 90% confidence range for the parameter.

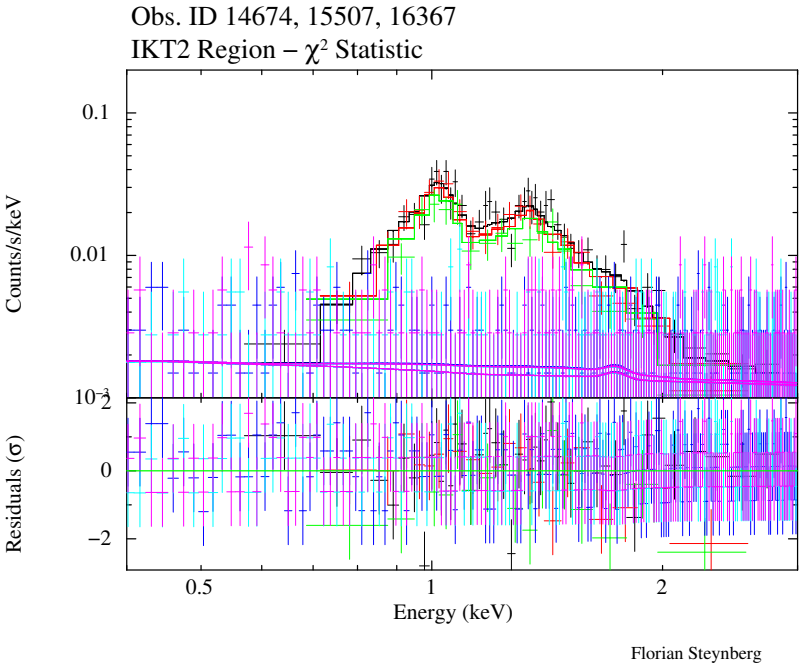

Figure 5: Spectral fit for the IKT2 Region with with a single vapec component and Gaussian statistic using the ACIS-I observations (Obs. IDs 14674, 15507, 16367). The bottom plot shows the residuals in terms of σ with error-bars of 1σ.

Parameter	min. value	best-fit value	max. value
kT [keV]	0.509252	0.547481	0.603751
Ne	5.4	5.98569	17.3
Mg	1.8	2.35607	6.5
norm.	4.8×10^{-5}	1.25447×10^{-4}	1.4×10^{-4}

Table 5: Parameter values for the spectral fit of the IKT2 region with a single vapec component and Gaussian statistic using the ACIS-I observations (Obs. IDs 14674, 15507, 16367). The minimum and maximum values give the 90% confidence range for the parameter.

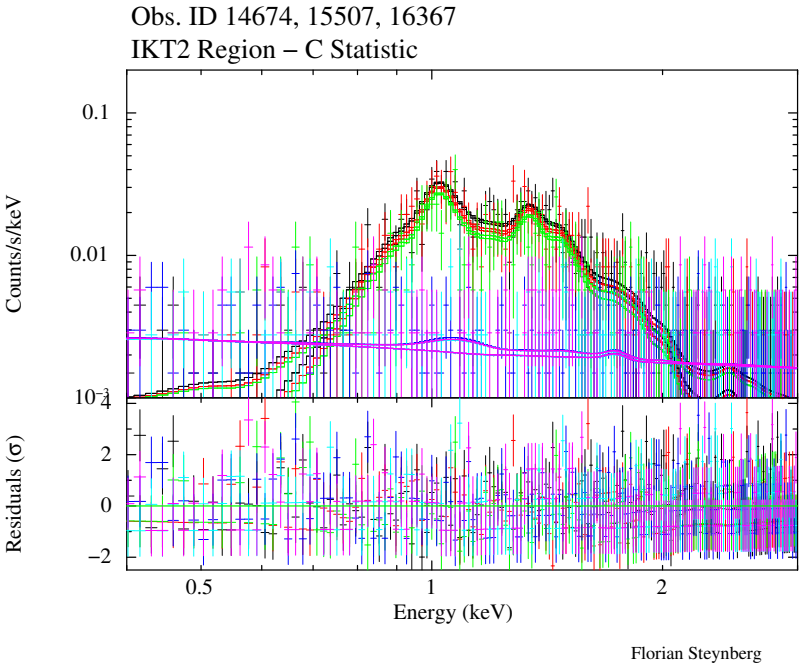

Figure 6: Spectral fit for the IKT2 Region with with a single vapec component and Poisson statistic using the ACIS-I observations (Obs. IDs 14674, 15507, 16367). The bottom plot shows the residuals in terms of σ with error-bars of 1σ.

Parameter	min. value	best-fit value	max. value
kT [keV]	0.552236	0.612143	0.67629
Ne	2.36185	3.94680	6.89001
Mg	1.27826	1.87077	2.92785
norm.	1.34844×10^{-4}	1.99293×10^{-4}	2.7208×10^{-4}

Table 6: Parameter values for the spectral fit of the IKT2 region with a single vapec component and Poisson statistic using the ACIS-I observations (Obs. IDs 14674, 15507, 16367). The minimum and maximum values give the 90% confidence range for the parameter.

Erklärung:

Hiermit bestätige ich, dass ich diese Arbeit selbstständig und nur unter Verwendung der angegebenen Hilfsmittel angefertigt habe.

_____ _____